Indonesian Journal of Science & Technology

Journal homepage: http://ejournal.upi.edu/index.php/ijost/

# Parametric Rotor Innovation for Gravitational Vortex Turbines: Advancing Clean Energy through Integrated Computational Fluid Dynamics (CFD)Simulation and Experimentation to Support the Sustainable Development Goals (SDGs)

*Pérez-Rodriguez Andrés Julián[1,*], Juan D. Pérez[2], Flórez-Arango Santiago[2], Jorge Andrés Sierra Del Rio[2]*

[1]Universidad Católica de Oriente, Rionegro, Colombia.
[2] Instituto Tecnológico Metropolitano, Medellín, Colombia.
* Correspondence: E-mail: ajperez@uco.edu.co

## ABSTRACT

This study aims to optimize the rotor design of gravitational vortex turbines through an integrated approach combining parametric modeling, computational fluid dynamics (CFD), and experimental validation. The rotor geometry was formulated using velocity triangle theory and refined using a CFD-based evaluation of flow behavior across multiple turbulence models. To ensure accurate comparisons, experimental tests were conducted under controlled flow conditions, and mechanical losses due to bearing friction were measured and accounted for. The simulation results demonstrated strong agreement with empirical data, validating the effectiveness of the proposed design. By enhancing energy conversion efficiency while minimizing environmental impact, this research supports the development of decentralized, renewable micro-hydropower systems. The findings contribute to the advancement of Sustainable Development Goals (SDGs).



## ARTICLE INFO

***Article History:***
*Submitted/Received 05 Jun 2025*
*First Revised 02 Jul 2025*
*Accepted 04 Sep 2025*
*First Available Online 06 Sep 2025*
*Publication Date 01 Dec 2026*

***Keyword:***
*Computational fluid dynamics,*
*Gravitational vortex turbine,*
*Hydropower,*
*Renewable energy,*
*Rotor optimization.*

## 1. INTRODUCTION

The global population and economic growth have intensified attention toward renewable energy sources, particularly highlighting hydropower as a key resource aligned with the United Nations' Sustainable Development Goals (SDGs) (see https://unstats.un.org/sdgs/report/2023/The-Sustainable-Development-Goals-Report-2023_Spanish.pdf). However, current efforts remain insufficient to meet the 2030 targets, revealing an urgent need to implement innovative renewable technologies with reduced environmental and social impacts. Although hydropower is a renewable source that avoids combustion processes, traditional implementation through large-scale hydroelectric projects results in significant alterations to surrounding terrestrial and aquatic ecosystems [1], as well as social issues related to forced displacement and community conflicts caused by flooding [2]. In response to these challenges, there is a growing interest in small-scale hydropower technologies that allow for efficient, renewable, and socially inclusive energy generation with minimal impacts [3].

In this context, the gravitational vortex turbine (GVT), developed in 2004, has gained attention due to its constructive simplicity, low economic and environmental cost, and capability for small-scale energy generation (pico-generation) (see Zotlöterer patent in 2004 regarding Hydroelectric power plant (Patent No. WO2004061295A2)). The GVT harnesses the motion of a gravity-induced vortex in a rotation chamber to drive a rotor at its core, while also allowing the free passage of aquatic species without compromising their survival. Additionally, its construction can be carried out using accessible materials with low environmental impact [4]. GVT efficiency shows high sensitivity to changes in its geometric parameters, with different performances observed depending on the specific rotor configuration implemented [5,6]. Several studies have explored innovative geometric alternatives, including straight and curved blades, multiple rotors, and optimized configurations to harness vertical flows, highlighting a theoretical gap regarding vortex behavior in the presence of a rotor [7-11].

To properly analyze the behavior of these gravity-induced vortical flows in GVTs, numerical methods such as computational fluid dynamics (CFD) and advanced experimental techniques like Particle Image Velocimetry (PIV) are commonly employed [12-14]. However, few studies have integrated both methodologies to optimize rotor design based on a detailed analysis of the velocity triangle applied to swirling flows, a methodology that has proven effective in other types of hydraulic turbines [15,16]. In this research, a specific geometry of a GVT is analyzed, based on a conical chamber designed to induce and stabilize a gravitational vortex (**Figure 1**). This configuration includes a rectangular inlet channel, a main conical tank, and a lower discharge orifice that ensures stable vortex formation. The dimensions and specific geometric parameters used are summarized in **Table 1**.

The selection of this GVT geometry was based on various numerical and experimental studies available in the literature. These studies have demonstrated that a conical tank geometry optimizes turbine performance by improving the tangential velocity of the flow [5,17,18].

DOI: https://doi.org/10.17509/ijost.v11i3.90012
p- ISSN 2528-1410 e- ISSN 2527-8045

**Table 1.** Main geometric parameters for the turbine.

| Parameter | Description | Value | Units |
|---|---|---|---|
| $H_c$ | Height of the inlet channel | 283 | mm |
| $L_c$ | Length of the inlet channel | 759 | mm |
| $H_{cd}$ | Height of the discharge chamber | 786 | mm |
| $H_r$ | Height of the rotor | 659.5 | mm |
| $D_{out}$ | Outlet diameter | 54 | mm |
| $W_c$ | Width of the inlet channel | 198 | mm |
| $\gamma$ | Wrap-around angle | 89.95 | ° |
| $D_{cd}$ | Upper chamber diameter | 500 | mm |

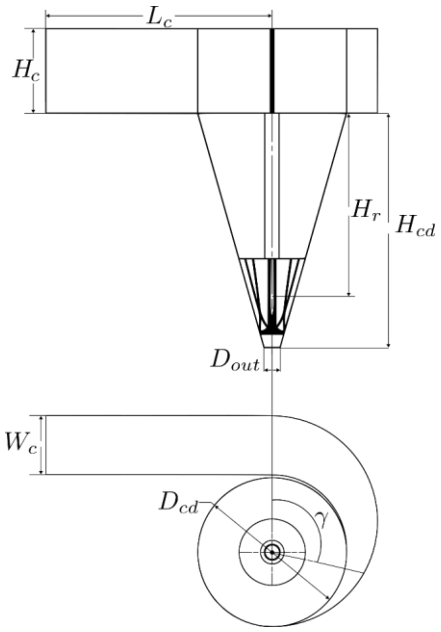


**Figure 1.** Main geometric parameters for the turbine.

## 2. METHODS

### 2.1. Rotor Design and Parametric Modeling

For the development of this study, a rotor design is proposed based on the fourth hydro-rotor [19]. This design is modifiable and allows the resizing of geometric parameters such as height, top and bottom radii, twist angle, and concavity. To this end, a parametric mathematical function was developed to describe the radius of a blade, using the next two principles to ensure that the rotor remains similar to its original model:

(i) The variation of *Z* is not constant with the variation of $\theta$ $\left(\frac{d^2Z}{d\theta^2} \neq 0\right)$.

(ii) The twist angle of each blade equals 2π radians divided by the number of blades $\left(\gamma = \frac{2\pi}{n}\right)$.

The parametric design used for this study is presented in Equations (1),(2), and (3).

$$z(t) = \frac{h_r\sqrt{2}}{2}\left(t + \sqrt{\left(t - \frac{\sqrt{2}}{2}\right)^2 + e^a} - \sqrt{\frac{1}{2} + e^a}\right) \quad (1)$$

$$\theta(t) = -\gamma\sqrt{2}\left(t - \sqrt{\left(t - \frac{\sqrt{2}}{2}\right)^2 + e^a} + \sqrt{\frac{1}{2} + e^a}\right) \quad (2)$$

$$r(t)\ \frac{\sqrt{2}(r_{up} - r_{down})}{2} z(t)\ r_{down} \quad (3)$$

DOI: https://doi.org/10.17509/ijost.v11i3.90012
p- ISSN 2528-1410 e- ISSN 2527-8045

where *z* is the height parameter, $\theta$ is the sweep angle in cylindrical coordinates, *r* is the variable rotor radius, *t* is the parameter ranging from 0 to $\sqrt{2}$, and *a* is the parameter controlling the curvature of the blade. The parameter $h_r$ is defined as 25 cm to maximize the use of the available 3D printing volume. The rotor selected for this study, shown in **Figure 2**, features a specific 4-blade configuration and an incidence angle ($\alpha$) of -3 degrees. This design aims to maximize the torque generated by the rotor and consequently improve the overall hydraulic efficiency of the system. The specific blade geometry was defined using the aforementioned parametric equations, enabling precise control of blade curvature via *a* parameter.

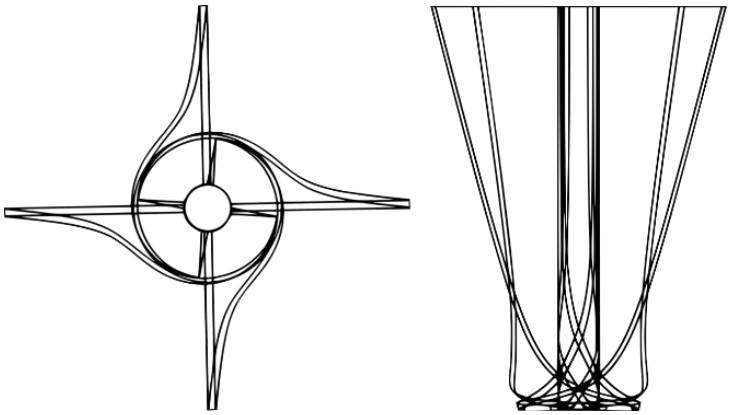

**Figure 2.** Design of the parametric runner.

For this analysis, the top surface (blue) is assumed to be the inlet to the control For this study, efficiency is calculated using Equation (4), and for its maximization, it is necessary to maximize the torque generated in the rotor, which can be calculated using the angular momentum equation presented in Equation (5).

$$\eta = \frac{\tau\omega}{QgH\delta} \tag{4}$$

$$\tau = \oint r \times V \cdot (V \cdot \hat{n})\delta dA \tag{5}$$

where $\eta$ corresponds to the efficiency, $\tau$ represents total torque, $\omega$ represents angular velocity, $Q$ corresponds to the total flow rate, $g$ is the acceleration of gravity, $H$ is the total head, and $\delta$ corresponds to the density of the water. $\boldsymbol{r}$ represents the vector from the rotor axis to each point in the analyzed surface; $\boldsymbol{V}$ is the velocity vector of the flow; $\hat{\boldsymbol{n}}$ is the normal vector perpendicular to the analyzed surface; and *A* is the area of each surface. The control surface selected for this analysis is shown in **Figure 3**.

Volume, and the inner surface (pink) as the outlet. The lateral surface (orange), which coincides with the chamber wall, does not contribute to torque generation in the rotor or domain (**Figure 3**). With the domain established, Equation (5) can be represented arithmetically as shown in Equation (6).

$$\tau = \int_0^{2\pi}\int_0^{r_1} r \cdot \boldsymbol{r} \times V_1 \cdot (V_1 \cdot \hat{\boldsymbol{n}})\delta dr d\theta - \int_0^{2\pi}\int_0^{r_2} r \cdot \boldsymbol{r} \times V_2 \cdot (V_2 \cdot \hat{\boldsymbol{n}})\rho dr d\theta$$

$$= \int_0^{2\pi}\int_0^{r} r^2 {V_1}^2 \cos(\theta_{\theta_1})\cos(\theta_{z_1})\,\rho dr d\theta - \int_0^{2\pi}\int_0^{r} r^2 {V_3}^2 \cos(\theta_{\theta_3})\cos(\theta_{z_3})\,\rho dr d\theta$$

$$= \frac{2\delta {V_1}^2 {r_1}^3 \pi}{3}\cos(\theta_{z_1})\cos(\theta_{\theta_1}) - \frac{2\delta {V_3}^2 {r_3}^3 \pi}{3}\cos(\theta_{z_3})\cos(\theta_{\theta_3}) \tag{6}$$

where $\cos(\theta_z)$ is the directional cosine of the velocity vector angle along the rotor axis and $\cos(\theta_\theta)$ is the tangential directional cosine. The total velocity of the water at the top of the rotor can be calculated using Torricelli's equation, shown in Equation (7).

DOI: https://doi.org/10.17509/ijost.v11i3.90012
p- ISSN 2528-1410 e- ISSN 2527-8045

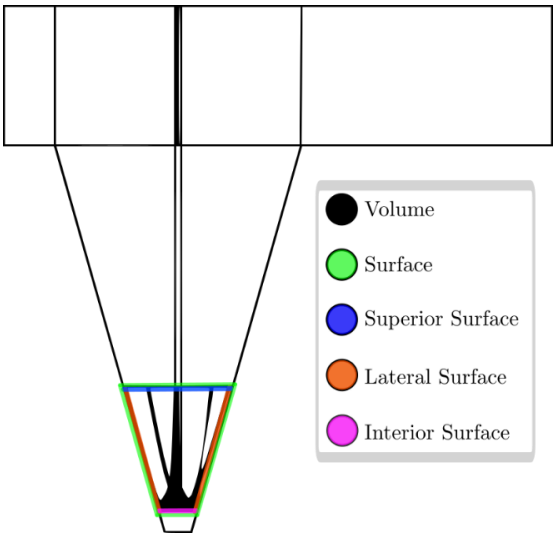


**Figure 3.** Main components of the GVT for the control volume details.

$$V = \sqrt{2gh} \tag{7}$$

Therefore, Equation (6) can be rewritten as shown in Equation (8).

$$\tau = \frac{4g\rho\pi}{3}\left(h_1 {r_1}^3 \cos(\theta_{z_1})\cos(\theta_{\theta_1}) - h_3 {r_3}^3 \cos(\theta_{z_3})\cos(\theta_{\theta_3})\right) \tag{8}$$

For this study, radial velocity is considered negligible in relation to tangential and axial velocities, so the directional cosines at the inlet are calculated using Equations (9) and (10):

$$\cos(\theta_z) = \frac{V_z}{\sqrt{{V_z}^2 + {V_\theta}^2}} = \sin(\theta_\theta) \tag{9}$$

$$\cos(\theta_\theta) = \frac{V_\theta}{\sqrt{{V_z}^2 + {V_\theta}^2}} = \sin(\theta_z) \tag{10}$$

where $V_Z$ and $V_\theta$ are the axial and tangential velocities, respectively. Since the analysis is performed under steady-state conditions, the average axial velocity can be calculated using the continuity principle and assuming constant density, while the tangential velocity is determined from the circulation $(\Gamma)$ obtained through CFD simulations using the expression proposed for vortex characterization [20], as shown in Equation (11).

$$V_\theta = \frac{\Gamma}{2\pi}\frac{2r}{r_m^2 + 2r^2} \tag{11}$$

where $r_m$ is the radius at which the vortex reaches its maximum velocity, assumed to be $0.7r$ according to literature [20]. On the other hand, the terms associated with the lower surface (outlet surface 3) can be controlled via the velocity triangles of the rotor shown in **Figure 4**. This figure shows both the general 3D representation and the planar projection of the velocity triangles at the rotor inlet and outlet to facilitate analysis. This figure presents the velocity triangles at three key positions in the GVT rotor: the inlet (**Figure 4(a)**), the internal blade passage (**Figure 4(b)**), and the outlet (**Figure 4(c)**). At the inlet, the absolute velocity of the flow ($V_1$), the blade velocity ($U_1$), and the relative velocity ($W_1$) define the angle of incidence and the energy input into the rotor. Within the blade passage (**Figure 4(b)**), the direction and magnitude of these velocity components change as energy is transferred from the fluid to the rotor. At the outlet (**Figure 4(c)**), the remaining absolute ($V_3$) and relative ($W_3$) velocities, along with blade velocity ($U_3$), determine how much energy has been effectively converted into torque and how much is lost with the exiting flow. Understanding these velocity relationships is crucial for optimizing rotor design and accurately calculating hydraulic efficiency based on momentum theory.

DOI: https://doi.org/10.17509/ijost.v11i3.90012
p- ISSN 2528-1410 e- ISSN 2527-8045

Angle $\alpha_1$ corresponds to the angle of $\theta_\theta$. Substituting Equations (8), (9), and (10) into Equation (4), and considering the velocity triangles, yields a hydraulic efficiency formulation for the machine, expressed in Equation (12).

$$\eta = \frac{4(W_1 h_1 A_1 \sin\alpha_1 \cos\alpha_1 - W_3 h_3 A_3 \sin\alpha_3 \cos\alpha_3)}{3Qh} \quad (12)$$

The relationships derived from the velocity triangles are presented in **Table 2**, and the correlation is in Equation (13).

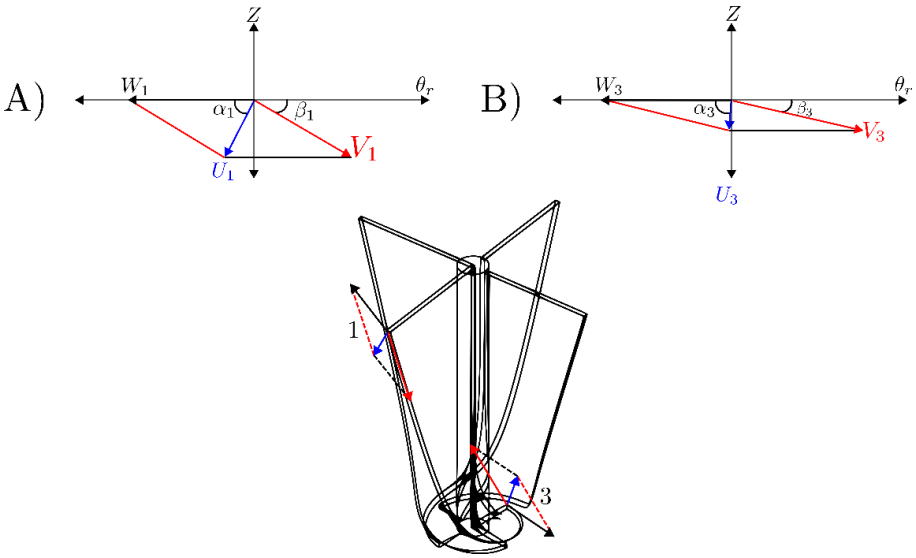


**Figure 4.** Velocity triangles at the inlet (a), inside the blade passage (b), and outlet (c) of the GVT rotor.

**Table 2.** Summary of velocity and flow equations.

| Equation | Expression | Eq. No. |
|---|---|---|
| *Velocity relationship* | $U \cdot \cos\alpha + V \cdot \cos\beta = W$ | (13) |
| *Velocity components* | $V \cdot \sin\beta = U \cdot \sin\alpha$ | (14) |
| *Flow rate equation* | $Q = AU \cdot \sin\alpha$ | (15) |
| *Velocity magnitude* | $V^2 = W^2 + U^2 - 2UW \cdot \cos\alpha$ | (16) |
| *Angular velocity* | $W = \omega r$ | (17) |

$$\mathrm{H} = \frac{4\mathrm{C}(-\mathrm{h}_3(\cos\alpha_3 + \cot\beta_3 \sin\alpha_3)\cos\alpha_3 + \mathrm{h}_1(\cos\alpha_1 + \cot\beta_1 \sin\alpha_1)\cos\alpha_1)}{3\mathrm{H_I}} \quad (13)$$

where $i$ defines which height is used and can take the values of 1 or 3, referring to the distance from the free water surface at the chamber inlet to positions 1 or 3 as shown in **Figure 4**. The constant $C$ is introduced to account for system losses. To reduce Equation (18) to independent terms only, it is necessary to express $\beta_1$ and $\beta_3$ in terms of $\alpha_1$ and $\alpha_3$. This is done using Equations (14) and (15), which were calculated using the partial derivative of the parametric equation used for the description of the rotor.

$$\beta_1(a,\gamma) = \tan^{-1}\left(\frac{r\gamma}{h_r} \cdot \frac{\sqrt{\frac{4}{1+2e^a}} - 2}{1 + \sqrt{\frac{1}{1+2e^a}}}\right) \quad (14)$$

$$\beta_2(a,\gamma) = \tan^{-1}\left(\frac{r\gamma}{h_r} \cdot \frac{2 + \sqrt{\frac{4}{1+2e^a}}}{\frac{1}{2}\sqrt{\frac{1}{1+2e^a}} - 1}\right) \quad (15)$$

From the last mathematical formulation, an estimate for efficiency can be obtained by predicting the directional components of the water at the inlet of the rotor. This prediction can be developed using CFD simulation. Notwithstanding, unlike other turbines, the GVT

DOI: https://doi.org/10.17509/ijost.v11i3.90012
p- ISSN 2528-1410 e- ISSN 2527-8045

extracts energy from a flow that cannot be analyzed unidirectionally, making it necessary to predict vortex behavior in advance to estimate $\alpha_1$ and, consequently, $\beta_1$. Through CFD simulation, it is possible to predict the physical variables involved in the rotational flow within the chamber using finite element analysis and numerical approximations of the time-averaged Navier–Stokes equations (RANS) [21,22]. The tangential velocity of water inside the turbine is approximated by calculating the circulation $(\Gamma)$ over the upper surface shown in **Figure 3** using Equation (16), developed in previous works [5,6].

$$\Gamma = \int \vec{\omega} \cdot dS \tag{16}$$

### 2.2. Mesh Generation, Solver Configuration

To conduct a detailed numerical study, nine CFD simulations were carried out in ANSYS CFX, aiming to compare three different turbulence models (*k-ε*, SST, and BSL) using the GCI methodology [23]. The goal is to select the model that best fits the experimental conditions of the study. Both the geometry and the interfaces that define the basic simulation parameters (**Figure 5**) were kept constant, regardless of the turbulence model simulated [18,24]. Two servers from the Instituto Tecnológico Metropolitano (ITM) were used for this task; their technical specifications are shown in **Table 3.**

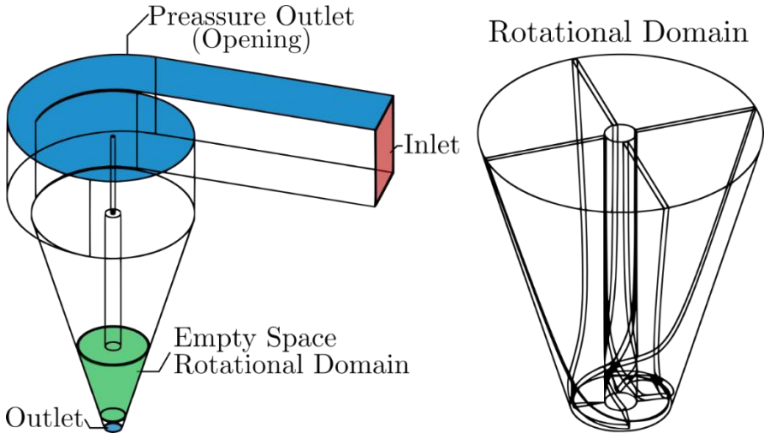


**Figure 5.** Domains for the CFD simulation of the GVT.

**Table 3.** Comparison of Computational Resources for CFD Simulations.

| Specification | Server 1: CLUSTER | Server 2: NEFTIS |
|---|---|---|
| | CPU / Processor | |
| *Brand and Model* | Intel Xeon E5-2690 | Intel Xeon Silver 4216 |
| *Number of Cores* | 16 | 32 |
| *Clock Speed (GHz)* | 2.9 | 2.10 |
| *Number of Threads* | 32 | 64 |
| | **RAM / Memory** | |
| *Total RAM Capacity (GB)* | 256 | 128 |
| *RAM Speed (MHz)* | DDR3 1333 | DDR4 1200 |
| | **Operating System** | |
| *OS Name and Version* | Windows 10 | Windows 10 |
| | **CFD Software / Version** | |
| *Software Name* | ANSYS CFX | ANSYS CFX |
| *Exact Version* | ANSYS R2 2022 | ANSYS R1 2024 |

DOI: https://doi.org/10.17509/ijost.v11i3.90012
p- ISSN 2528-1410 e- ISSN 2527-8045

The mesh used for the CFD simulations was generated using the ANSYS Meshing module, employing tetrahedral elements (**Figure 6**). To ensure the quality and reliability of the numerical results, different quality metrics were evaluated for the generated elements. **Table 4** presents the average values obtained for these metrics across the nine case studies [5].

**Table 4.** Mesh quality metrics for different levels of refinement.

| Mesh Level | Min Orthogonal Quality | Avg Orthogonal Quality | Max Skewness | Avg Skewness | Max Aspect Ratio | Avg Aspect Ratio |
|---|---|---|---|---|---|---|
| Fine | 0.09 | 0.75 | 0.9 | 0.24 | 14 | 1.85 |
| Medium | 0.11 | 0.82 | 0.9 | 0.28 | 15 | 1.83 |
| Coarse | 0.13 | 0.82 | 0.9 | 0.23 | 14.2 | 1.84 |

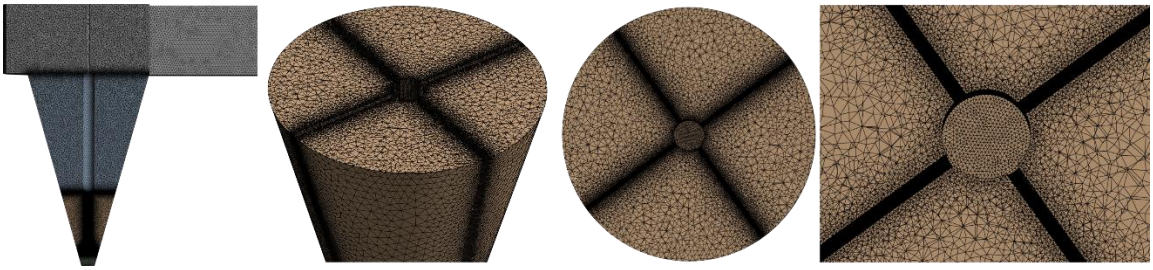

**Figure 6.** Mesh on the control volume.

The parameters used for configuring the CFD simulations in ANSYS CFX are summarized in **Table 5**. These parameters were carefully selected to accurately reflect the experimental conditions described in the previous section, thus ensuring proper numerical convergence in all analyzed cases. Additionally, the results obtained with the three evaluated turbulence models will be contrasted using the mesh independence methodology (GCI), ensuring the quality and reliability of the numerical study conducted [25].

**Table 5.** Parameters used in the CFD simulation configuration.

| Parameter | Value |
|---|---|
| Inlet velocity [m/s] | 0.0539 |
| Angular velocity [rad/s] | 11 |
| Reference pressure [atm] | 1 |
| Outlet pressures [atm] | 0 |
| Time step | 0.01 |
| Density ($\rho$) [kg/m$^3$] | 998.2 |
| Gravitational acceleration ($g$) [m/s$^2$] | 9.81 |
| Average Courant number | 12 |
| Surface tension [N/m] | 0.072 |
| Rotor interface type | Frozen Rotor |
| Pitch angle | 360 |

### 2.3. Experimental Methodology

#### 2.3.1. Experimental setup and parameters

For the development of the experimental tests, a setup was assembled in the GEA laboratory using available components (**Figure 7**). The system is primarily composed of an inlet channel and a discharge chamber made of transparent acrylic to allow visualization of vortex formation, specific sensors for accurate measurement of flow rate (SITRANS F M MAG

DOI: https://doi.org/10.17509/ijost.v11i3.90012
p- ISSN 2528-1410 e- ISSN 2527-8045

5100W) and torque (FUTEK USB 520/530), and a specially designed runner manufactured through 3D printing [26]. It is worth noting that the rotor was printed using a Creality Ki printer with PLA filament, 1.75 mm in diameter, 0.2 mm layer height, and 100% infill. The printing parameters included an extruder temperature of 220 °C and a bed temperature of 45 °C, ensuring the dimensional accuracy and surface quality required for the experimental tests. During the tests, a constant water flow rate of 2.5 and 3 L/s was maintained. The rotor's dynamic variables, including speed and torque, were recorded over 30 seconds after the flow reached a steady state (**Figure 8**). The key components of the experimental setup are summarized in detail in **Table 6** [27].

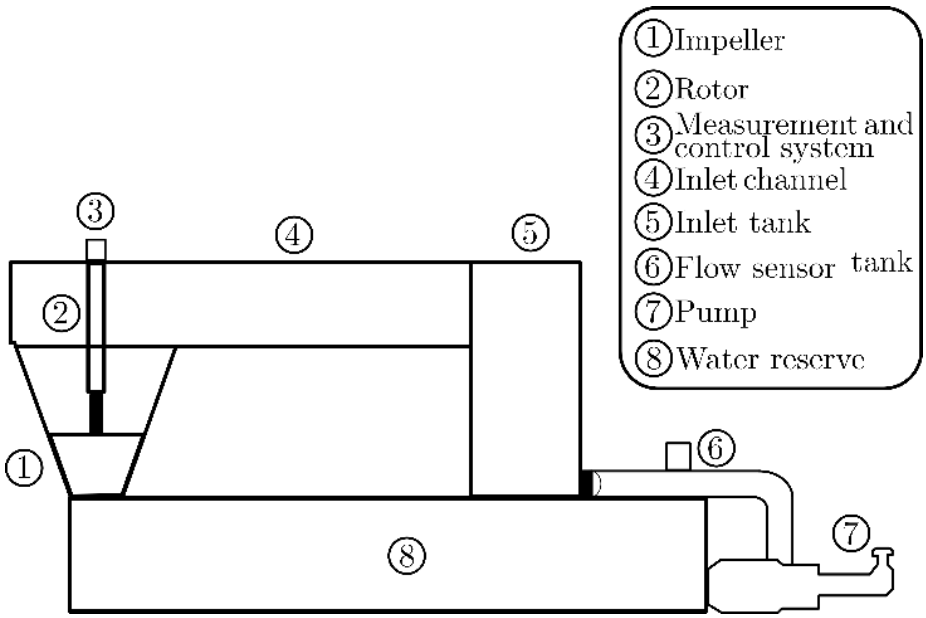


**Figure 7.** Elements of the experimental setup.

**Figure 8.** Experimental facilities.

DOI: https://doi.org/10.17509/ijost.v11i3.90012
p- ISSN 2528-1410 e- ISSN 2527-8045

Once the experimental setup was defined and validated, a comparison with the numerical study was carried out. The specific methodology and characteristics for this analysis and its results will be detailed in the following section.

**Table 6.** Components of the Measurement and Control System and Hydraulic Elements.

| Element | Sub-Element | Description |
|---|---|---|
| Measurement and Control System | Flow Sensor | SITRANS F M MAG 5100W |
| | Torque Sensor | FUTEK USB 520/530 |
| | CPU and Software | SENSIT software |
| Inlet Channel and Inlet Tank | Dimensions | Structures for controlled water routing, made of 5 mm-thick transparent acrylic<br>Height: 250 mm<br>Width: 250 mm<br>Length: 1250 |
| Water Reserve Tank | | Capacity of 2 $m^3$ |
| Pump | | IHM 30A-15W – IE2, controlled with a variable frequency drive |

### 2.3.2. Calculation of bearing losses

Due to the conditions of the experimental setup, specifically the state of the bearings coupled to the rotor shaft, it is necessary to consider friction losses when comparing the experimental results with the numerical data [28]. To quantify these losses, the experimental setup shown in **Figure 9** was used. In these tests, a constant speed of 100 RPM was maintained, equivalent to the simulation speed, and the rotor deceleration was recorded after interrupting the airflow. Thanks to the torque sensor, it was possible to determine the angular acceleration from the variation in angular velocity over time [29].

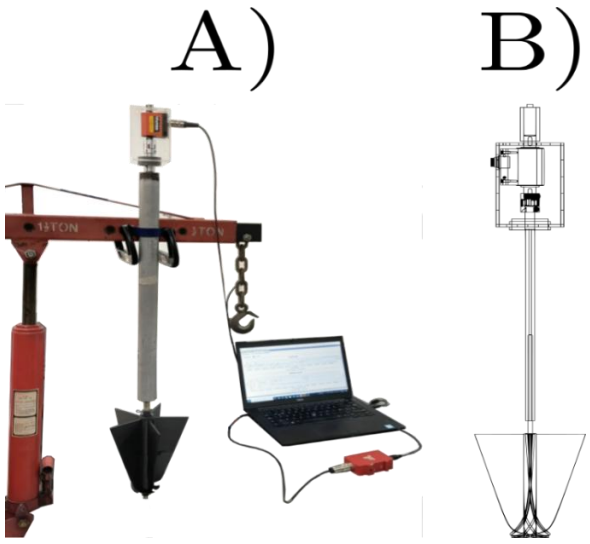


**Figure 9.** Experimental setup for determining bearing losses. (A) Physical assembly used for testing, and (B) Schematic diagram of the measurement system.

The angular acceleration is obtained from Equation (17).

$$\alpha = \frac{\Delta\omega}{\Delta t} \tag{17}$$

DOI: https://doi.org/10.17509/ijost.v11i3.90012
p- ISSN 2528-1410 e- ISSN 2527-8045

where $\Delta\omega$ is the change in angular velocity and $\Delta t$ is the time interval between measurements. The moment of inertia of the shaft, modeled as a solid cylinder of mass $m$, length $L$, and radius $R$, is expressed as Equation (18).

$$\mathrm{I} = \frac{1}{12}mL^2 + \frac{1}{4}mR^2 \quad (18)$$

The friction torque is calculated by multiplying this moment of inertia by the absolute value of the angular acceleration (Equation (19)).

$$T_{Fric} = I|\alpha| \quad (19)$$

Finally, the power lost due to friction at 100 RPM is determined by Equation (20).

$$P_{Fric} = T_{Fric}\omega_{100} \quad (20)$$

**Table 7** summarizes all the experimental parameters needed to quantify friction losses in the rotor shaft bearings [30]. This corrected torque value will be used for comparison between experimental and numerical results. It is emphasized that, due to the state of the bearings, this value is essential for accurately describing the experimental results, as friction losses in the bearings account for approximately 11 % of the measured net torque. In this way, a corrected experimental torque of 0.664 Nm is obtained, which is essential for accurately accounting for the losses induced by the condition of the bearings.

This corrected torque value will be used for comparison between experimental and numerical results. It is emphasized that, due to the state of the bearings, this value is essential for accurately describing the experimental results, as friction losses in the bearings account for approximately 11% of the measured net torque. In this way, a corrected experimental torque of 0.664 Nm is obtained, which is essential for accurately accounting for the losses induced by the condition of the bearings.

**Table 7.** Experimental parameters and calculated values to quantify friction losses.

| Parameter | Symbol | Value | Units |
|---|---|---|---|
| *Rotor shaft mass* | $m$ | 0.895 | $kg$ |
| *Moment of inertia* | $I$ | $6.042e-02$ | $kgm^2$ |
| *Average angular acceleration* | $\alpha$ | $-1.102$ | $\frac{rad}{s^2}$ |
| *Friction torque* | $T_{Fric}$ | 0.066 | $Nm$ |
| *Power loss* | $P_{Fric}$ | 0.697 | $W$ |
| *Net experimental torque* | $T_{ExpN}$ | 0.597 | $Nm$ |
| *Corrected experimental torque* | $T_{ExpC}$ | 0.663 | $Nm$ |

## 3. RESULTS AND DISCUSSION

This section presents both the numerical analyses and the efficiency evaluation. First, the numerical results obtained from simulations using three turbulence models (*k-ε*, SST, and BSL) are detailed, with emphasis on the prediction of rotor torque; this is achieved through the evaluation of convergence using the Richardson extrapolation method and the calculation of the GCI [31]. This analysis allows the identification of differences in stability and result dispersion among the various models. On the other hand, the efficiency of the turbine is addressed through a direct comparison between numerical and experimental values, describing the methods used to calculate the available power and the shaft power [5], which are essential to determine the system's performance, reaching a maximum experimental value close to 50.6%.

DOI: https://doi.org/10.17509/ijost.v11i3.90012
p- ISSN 2528-1410 e- ISSN 2527-8045

### 3.1. Numerical and GCI results

Once the configuration parameters for the numerical simulations were defined, the cases were executed for the three turbulence models considered (*k-ε*, SST, and BSL). The results obtained for rotor torque in the time interval between 34 and 37 seconds are summarized in **Table 8** and illustrated in **Figure 10**. In the finest mesh, composed of 9,974,357 elements, the BSL model yields the highest torque value at 0.73 Nm, while the *k-ε* model records the lowest value of 0.613 Nm. The SST model presents intermediate values with 0.661 Nm. This trend remains consistent across the different mesh configurations evaluated, considering in all cases a constant inlet velocity of 0.0539 m/s.

**Table 8.** Torque results for different mesh configurations and turbulence models.

| Elements | K−ε | SST | BSL |
|---|---|---|---|
| 9,974,357 | 0.613 | 0.661 | 0.73 |
| 3,610,398 | 0.604 | 0.632 | 0.62 |
| 1,295,088 | 0.598 | 0.577 | 0.612 |

The analysis using the Richardson extrapolation method enables the evaluation of numerical convergence and stability for each model in torque prediction, based on the calculation of the Grid Convergence Index (GCI) for fine and coarse meshes. In the case of the k-ε model, very close values are observed, with a GCI of 7.341% in the fine mesh and 7.450% in the coarse mesh, indicating stable and consistent convergence. In contrast, the SST model exhibits significantly higher indices, with 38.124% for the fine mesh and 39.873% for the coarse mesh, suggesting greater result dispersion. The BSL model presents the highest GCI values, reaching 48.493% on the fine mesh and 57.097% on the coarse mesh (**Figure 11**), indicating strong mesh dependence and potential convergence issues by this criterion [6].

However, when considering only the minimum relative error within the experimental uncertainty range, the BSL model shows the best performance, with an error of just 4.6%, followed by the SST model at 9.1%, and the k-ε model at 11.7%. These results suggest that, under ideal conditions within the uncertainty band, the BSL model approximates the corrected experimental torque value of 0.6025 Nm more closely than the others. Nonetheless, this agreement does not guarantee the model's reliability, as its high GCI indicates a strong sensitivity to mesh resolution, raising concerns about the robustness and generalizability of its predictions under varying simulation conditions (**Figure 12**).

Therefore, these findings underscore the importance of jointly considering both convergence indicators and direct comparison with experimental data. A seemingly accurate prediction may be misleading if it is not supported by a numerically stable and mesh-independent solution [32].

DOI: https://doi.org/10.17509/ijost.v11i3.90012
p- ISSN 2528-1410 e- ISSN 2527-8045

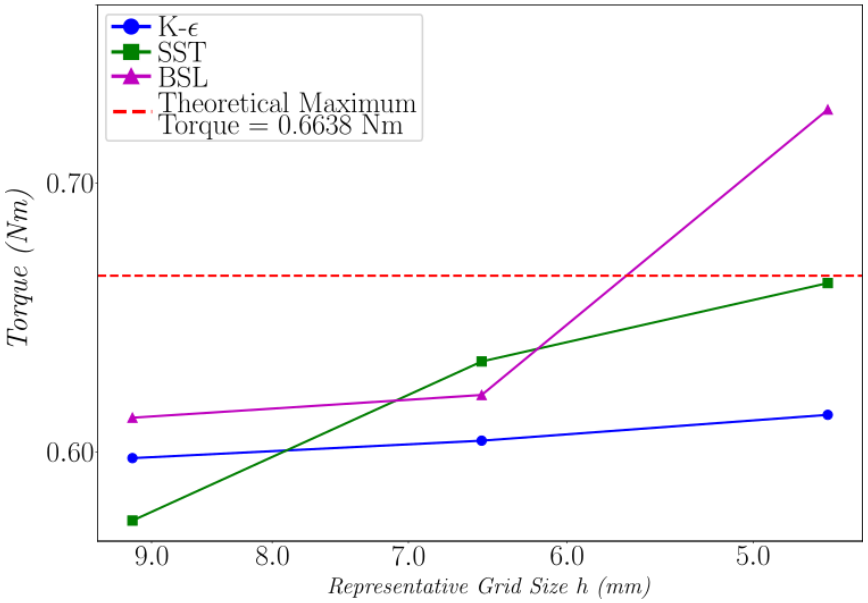


**Figure 10.** Numerical results by model.

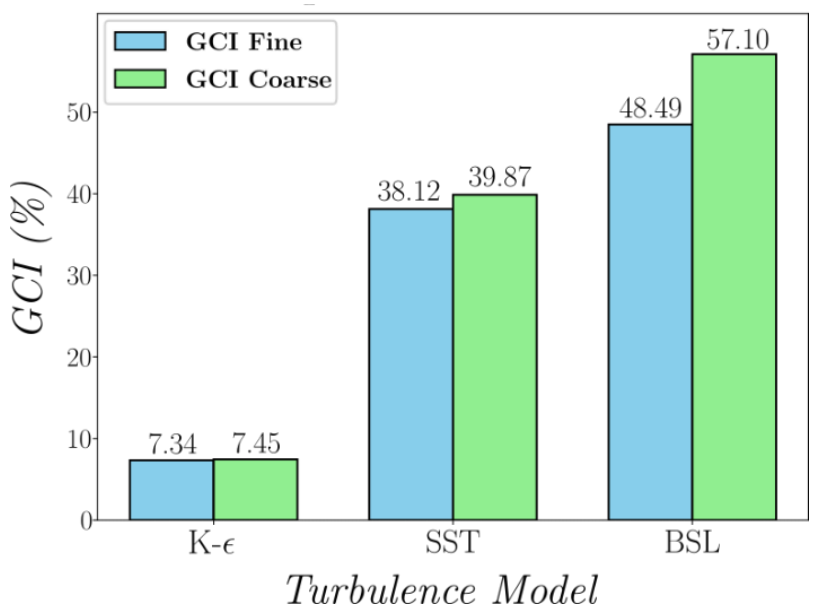


**Figure 11.** Richardson extrapolation method and Grid Convergence Index.

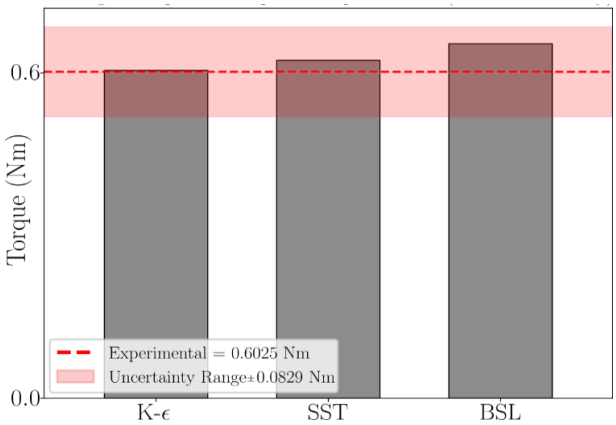


**Figure 12.** The average value of the numerical results of each model is relative to the experimental value.

DOI: https://doi.org/10.17509/ijost.v11i3.90012
p- ISSN 2528-1410 e- ISSN 2527-8045

### 3.2. Experimental Results

**Table 9** summarizes the main findings from four experimental tests (two performed at a flow rate of 2.5 L/s and two at 3.0 L/s). Each row presents the maximum power measured during the experiment, the angular speed at which the maximum torque was observed, and the best efficiency predicted by the correlation equations derived from the experimental data. These correlation equations obtained by fitting the relationship among torque, power, angular speed, and flow rate are valid exclusively for the tested conditions. Their purpose is to relate the useful power ($P_U$) and the hydraulic power ($P_H$). Thus, the efficiency $\eta$ can be predicted within the measured operating range (Equation (21)).

$$P_U = T\omega \tag{21}$$

where $\omega$ is the angular speed of the rotor and $T$ is the torque (Equation (22)).

$$P_H = \rho g H_T Q \tag{22}$$

where the total head is $H_T$ = 0.488 m, and all other relevant hydraulic and operational parameters such as fluid properties, flow conditions, and rotor speed are summarized in **Table 5**. The flow rate ($Q$) is derived from the inlet velocity and cross-sectional area, as detailed therein. A representative form of the power speed correlation used in these tests, for instance, can be written as Equation (23).

$$\tau = a + \frac{\boldsymbol{b}}{\boldsymbol{\omega^c}} \tag{23}$$

where $\tau$ is the torque, and $\omega$ is the angular speed. By substituting $\tau$ into (Equation (24)).

$$P = \omega\tau \tag{24}$$

We obtained Equation (25):

$$P(\omega) = \left(a + \frac{b}{\omega^c}\right) \tag{25}$$

This expression shows how the power output depends on the rotor's angular speed. The constants $a$, $b$, and $c$ were determined from experimental data and are valid only within the specific range of flow rates (2.5 - 3.0 L/s) and the geometrical parameters tested. The values obtained from the best-performing case are: $a$ = 0.6927, $b$ = -0.6465, and $c$ = -2.0833. Test 3 in **Table 9** exhibits the best performance among the four tests, reaching the highest measured power of 13.262 W at a flow rate of 3.0 L/s. Moreover, for an angular velocity of 11 rpm, the measured torque in this test was 0.6025 Nm, with an associated uncertainty of ±0.0829 Nm. This torque value should be taken as the representative experimental result under these operating conditions.

**Table 9.** Test results of experiments.

| | Flow rate (L/s) | Maximum Measured Power (*W*) | Angular speed of max. measured torque (rad/s) | Best Efficiency (correlation) | Torque at max. power (N.m) | Torque at 11 rpm (N.m) |
|---|---|---|---|---|---|---|
| 1 | 2.5 | 10.089 | 16.650 | 0.399 | 0.470 | 0.556 |
| 2 | 2.5 | 10.347 | 17.279 | 0.390 | 0.433 | 0.523 |
| 3 | 3 | 13.262 | 21.468 | 0.347 | 0.463 | 0.597 |
| 4 | 3 | 10.863 | 17.907 | 0.337 | 0.469 | 0.596 |

DOI: https://doi.org/10.17509/ijost.v11i3.90012
p- ISSN 2528-1410 e- ISSN 2527-8045

### 3.3. Comparative Discussion

To contrast the numerical results with the experimental ones, **Figure 13** shows the efficiency percentage ($\eta$) for the turbine design. The efficiency is calculated using Equation (26).

$$\eta = \frac{P_O}{P_H} 100\% \quad (26)$$

where $P_O$ is the shaft power and $P_H$ is the available power. With these parameters, the overall performance of the turbine is estimated, whose maximum measured value is approximately 50.6%. In contrast, the numerical simulations carried out showed efficiencies ranging around similar values (48-52%, depending on the turbulence model and mesh refinement). Although the *BSL model* presented a relatively high Grid Convergence Index (GCI), it ended up providing torque and efficiency results closer to the experimental data than other models (e.g., *k-ε*). This behavior can be attributed to the BSL model's better capability to represent the fluid dynamic behavior occurring in the vortex chamber, even when the dispersion according to the GCI is greater. The main discrepancies between numerical and experimental values can be explained by various causes, such as vortex and free surface flow, experimental limitations, or assumptions in the simulation setup. Nevertheless, the fact that the BSL model better reproduces the results, despite its higher GCI, highlights the relevance of comparing the physical accuracy of simulations with experimental data, in addition to analyzing mesh convergence. In other words, a favorable GCI does not necessarily guarantee the most accurate prediction, especially in flows with high circulation.

### 3.4. Discussion and Future Work

The GVT is reaffirmed in this study as a promising technology for small-scale renewable energy generation, particularly in geographically remote or underserved areas where conventional electrification infrastructure is limited or economically unfeasible [33,34]. Its design simplicity, low ecological footprint, and adaptability make it well-suited for decentralized energy applications. Within this context, optimizing hydrokinetic turbine components is essential for maximizing energy conversion efficiency from natural water flows. This research confirms that rotor geometry, specifically when derived from parametric curves and adjusted to circulation characteristics, plays a decisive role in determining overall turbine performance [35,36].

The proposed rotor configuration demonstrated improved hydraulic efficiency in both numerical simulations and physical testing, with performance results aligning well between experimental measurements and CFD predictions [37]. This alignment reinforces the effectiveness of integrating computational modeling with empirical validation. Moreover, the analysis revealed that physical constraints in the test setup (especially bearing friction) had a notable impact on performance, highlighting the importance of mechanical design considerations in real-world implementations.

From a broader perspective, these findings directly contribute to the United Nations SDGs. The advancement of clean and affordable energy technologies aligns with SDG 7, while the application of computational and experimental innovation supports SDG 9. Furthermore, by promoting the use of localized, non-polluting energy systems that reduce dependency on fossil fuels, this work contributes meaningfully to SDG 13 on climate action. Indeed, this study adds new information regarding support for sustainable energy and SDGs as reported elsewhere [38-55].

Future work should focus on holistic optimization of the entire GVT system. This includes redesigning additional components such as the inlet channel, the vortex chamber, and the

DOI: https://doi.org/10.17509/ijost.v11i3.90012
p- ISSN 2528-1410 e- ISSN 2527-8045

outlet to ensure seamless integration with the rotor's geometric characteristics. Implementing multi-variable optimization algorithms (based on circulation, vorticity, and turbulence modeling) could enable more precise control of internal flow behavior and further enhance energy recovery. In addition, real-world deployment studies in off-grid communities could help validate long-term performance, reliability, and social impact, further solidifying the role of GVTs as practical contributors to sustainable energy infrastructure.

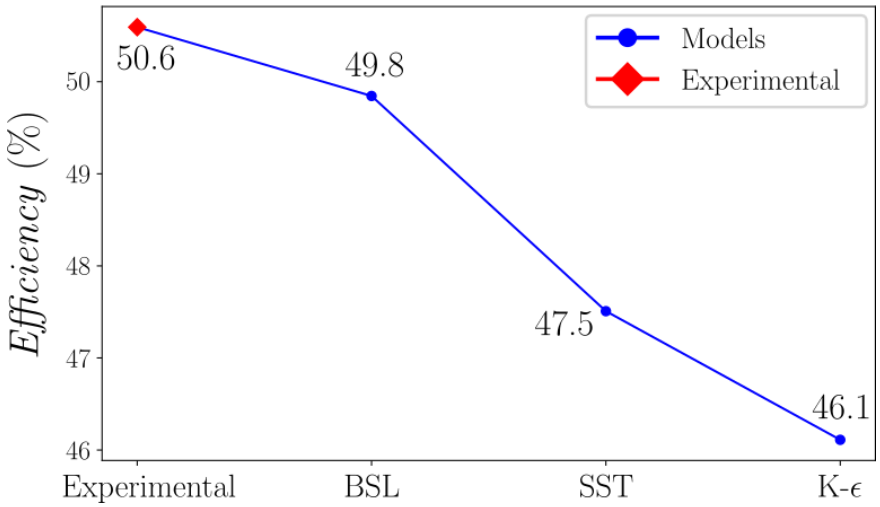


**Figure 13.** Comparison of experimental efficiency with numerical models.

## 4. Conclusion

This study proposed and validated a novel rotor design for a GVT using a combined approach of parametric modeling, CFD, and experimental testing. The proposed rotor, designed through mathematical parameterization to optimize blade curvature and flow interaction, achieved a maximum experimental efficiency of 50.6%, which is competitive with or superior to values reported in prior studies. Numerical simulations using three turbulence models ($k$-$\varepsilon$, SST, and BSL) were evaluated, with the BSL model demonstrating the closest agreement to experimental results despite exhibiting higher sensitivity to mesh resolution. These findings highlight the importance of not only ensuring numerical convergence but also validating model predictions against experimental data. The corrected torque and efficiency values accounted for bearing friction losses, ensuring accurate performance assessment. Overall, the results confirm that optimized rotor geometry significantly enhances energy conversion in GVT systems. Future work should focus on the integrated optimization of the rotor, inlet channel, and tank geometry, as well as the application of advanced optimization algorithms based on circulation and vorticity parameters. This study supports SDGs.

## 5. ACKNOWLEDGMENT

We acknowledge the financial support provided by the announcement No. 890 de 2020 "Convocatoria para el fortalecimiento de CTeI en Instituciones de Educación Superior (IES) Públicas 2020" (Contract No. 2022-0453).

## 6. AUTHORS' NOTE

The authors declare that there is no conflict of interest regarding the publication of this article. The authors confirmed that the paper was free of plagiarism.

DOI: https://doi.org/10.17509/ijost.v11i3.90012
p- ISSN 2528-1410 e- ISSN 2527-8045

## 7. REFERENCES


[1] Sun, S. (2023). Development of hydropower and the environmental impacts of hydroelectric dam construction in China. *E3S Web of Conferences*, *393*, 01032.

[2] Del Bene, D., Scheidel, A., and Temper, L. (2018). More dams, more violence? A global analysis of resistances and repression around conflictive dams through co-produced knowledge. *Sustainable Science*, *13*(3), 617–633.

[3] Williamson, S. J., Lubitz, W. D., Williams, A. A., Booker, J. D., and Butchers, J. P. (2020). Challenges facing the implementation of pico-hydropower technologies. *Journal of Sustainable Research*, *2020*, 0003.

[4] Alzamora Guzmán, V. J., Glasscock, J. A., and Whitehouse, F. (2019). Design and construction of an off-grid gravitational vortex hydropower plant: A case study in rural Peru. *Sustainable Energy Technologies and Assessments*, *35*, 131–138.

[5] Velásquez, L., Posada, A., and Chica, E. (2022). Optimization of the basin and inlet channel of a gravitational water vortex hydraulic turbine using the response surface methodology. *Renewable Energy, 187*, 508–521.

[6] Velásquez, L., Posada, A., and Chica, E. (2023). Surrogate modeling method for multi-objective optimization of the inlet channel and the basin of a gravitational water vortex hydraulic turbine. *Applied Energy, 330*, 120357.

[7] Venukumar, A., Nandakumar, M., Venkateswara Rao, M., and Kumar, S. M. (2015). Run-of-the-river micro hydroelectric power generation from artificially induced vortices. *Power Research*, *11*(4), 741-750.

[8] Dhakal, S., Nakarmi, S., Pun, P., Thapa, A. B., and Bajracharya, T. R. (2013). Development and testing of runner and conical basin for gravitational water vortex power plant. *Journal of the Institute of Engineering*, *10*(1), 140–148.

[9] Wichian, P., and Suntivarakorn, R. (2016). The effects of turbine baffle plates on the efficiency of water free vortex turbines. *Energy Procedia*, *100*, 198–202.

[10] Ullah, R., Cheema, T. A., Saleem, A. S., Ahmad, S. M., Chattha, J. A., and Park, C. W. (2019). Performance analysis of multi-stage gravitational water vortex turbine. *Energy Conversion and Management*, *198*, 111788.

[11] Ullah, R., Cheema, T. A., Saleem, A. S., Ahmad, S. M., Chattha, J. A., and Park, C. W. (2020). Preliminary experimental study on multi-stage gravitational water vortex turbine in a conical basin. *Renewable Energy*, *145*, 2516-2529.

[12] Mulligan, S., Creedon, L., Casserly, J., and Sherlock, R. (2018). An improved model for the tangential velocity distribution in strong free-surface vortices: An experimental and theoretical study. *Journal of Hydraulic Research*, *56*(6), 757–771.

[13] Shabara, H. M., Yaakob, O. B., Ahmed, Y. M., and Elbatran, A. H. (2015). CFD simulation of water gravitation vortex pool flow for mini hydropower plants. *Jurnal Teknologi*, *74*(5), 77–81.

[14] Shabara, H. M., Yaakob, O. B., Ahmed, Y. M., Elbatran, A. H., and Faddir, M. S. M. (2015). CFD validation for efficient gravitational vortex pool system. *Jurnal Teknologi*, *74*(5), 97–100.

[15] Perez-Rodriguez, A. J., Del Rio, J. S., Grisales-Noreña, L. F., and Galvis, S. (2022). Optimization of the efficiency of a Michell-Banki turbine through the variation of its geometrical parameters using a PSO algorithm. *WSEAS Transactions on Heat and Mass Transfer*, *17*, 45–53.


DOI: https://doi.org/10.17509/ijost.v11i3.90012
p- ISSN 2528-1410 e- ISSN 2527-8045

[16] Vaz, D. A. T. D. do Rio, Vaz, J. R. P., and Silva, P. A. S. F. (2018). An approach for the optimization of diffuser-augmented hydrokinetic blades free of cavitation. *Energy for Sustainable Development*, *45*, 142–149.

[17] Velásquez García, L., Rubio-Clemente, A., and Chica, E. (2022). Runner optimal position in a gravitational water vortex hydraulic turbine with a spiral inlet channel and a conical basin. *Renewable Energies and Power Quality Journal*, *20*, 248.

[18] Velásquez, L., Rubio-Clemente, A., and Chica, E. (2024). Numerical and experimental evaluation of the performance of agravitational vortex turbine rotor. *Renewable Energy and Power Quality Journal*, *22*(4), 133-137.

[19] Jiang, Y., Raji, A. P., Raja, V., Wang, F., AL-bonsrulah, H. A. Z., Murugesan, R., and Ranganathan, S. (2022). Multi–disciplinary optimizations of small-scale gravitational vortex hydropower (SGVHP) system through computational hydrodynamic and hydro–structural analyses. *Sustainability*, *14*(2), 727.

[20] Hite, J. E., and Mih, W. C. (1994). Velocity of air-core vortices at hydraulic intakes. *Journal of Hydraulic Engineering*, *120*(3), 284–297.

[21] Alfonsi, G. (2009). Reynolds-averaged Navier-Stokes equations for turbulence modeling. *Applied Mechanics Reviews*, *62*(4), 040802.

[22] Liu, M., Jiang, C., Gao, G., Zhu, H., and Xu, L. (2024). Assessment of RANS turbulence models based on the cell-based smoothed finite element model for prediction of turbulent flow. *Engineering Analysis with Boundary Elements*, *168*, 105937.

[23] Monsalve-Cifuentes, O. D., Vélez-García, S., Sanín-Villa, D., and Revuelta-Acosta, J. D. (2024). Fluid-structure numerical study of an in-pipe axial turbine with circular blades. *Energies*, *17*(14), 3539.

[24] Burbano, A., Sierra, J., Correa, E., Ruiz, A., and Sanin, D. (2022). Numerical simulation of the inlet channel geometry influence in the torque generated at the gravitation water vortex turbine. *EUREKA: Physics and Engineering*, *6*, 106–119.

[25] Celik, I. B., Ghia, U., Roache, P. J., Freitas, C. J., Coleman, H., and Raad, P. E. (2008). Procedure for estimation and reporting of uncertainty due to discretization in CFD applications. *Journal of Fluids Engineering*, *130*(7), 078001.

[26] Rouway, M., Nachtane, M., Tarfaoui, M., Chakhchaoui, N., Omari, L. E. H., Fraija, F., and Cherkaoui, O. (2021). 3D printing: Rapid manufacturing of a new small-scale tidal turbine blade. *The International Journal of Advanced Manufacturing Technology*, *115*, 61–76.

[27] Betancour, J., Romero-Menco, F., Velásquez, L., Rubio-Clemente, A., and Chica, E. (2023). Design and optimization of a runner for a gravitational vortex turbine using the response surface methodology and experimental tests. *Renewable Energy*, *210*, 306–320.

[28] Wu, P. L., He, C. L., Chang, Z., Li, X. L., Ren, Z. Y., Li, D. Y., and Ren, C. Z. (2022). Theoretical calculation models and measurement of friction torque for rolling bearings: State of the art. *Journal of the Brazilian Society of Mechanical Sciences and Engineering*, *44*, 435.

[29] Campbell, J. B., and Schwarz, J. M. (2011). Precise measurement of velocity dependent friction in rotational motion using a falling mass. *European Journal of Physics*, *32*(5), 1323–1333.

[30] Zhou, J., Guo, Y., and Wang, D. (2015). Analysis on the load characteristics and coefficient of friction of angular contact ball bearing at high speed. *Tribology International*, *92*, 362–370.

[31] Kumar, S. M., Kumar, A., and Saini, R. P. (2013). Computational fluid dynamics (CFD) mesh independency technique applied to a Kaplan turbine draft tube. *Energy*, *58*, 272–280.

DOI: https://doi.org/10.17509/ijost.v11i3.90012
p- ISSN 2528-1410 e- ISSN 2527-8045

[32] Escalera, E., Morales, R., and Morales, R. (2011). Experimental and numerical simulations predictions comparison of power and efficiency in hydraulic turbine. *International Journal of Rotating Machinery*, *2011*, 146054.
[33] Akbaş, B., Kocaman, A. S., Nock, D., and Trotter, P. A. (2022). Rural electrification: An overview of optimization methods. *Renewable and Sustainable Energy Reviews*, *156*, 111935.
[34] Kyawo, A., Khan, M. I., Chowdhury, S. I., and Rahaman, S. (2023). Assessing the feasibility of gravitational vortex turbines for sustainable energy production in remote hilly areas of Bangladesh. *Journal of Energy Research and Reviews*, *14*(4), 45–55.
[35] Haryadi, H., Subarjah, A. M., and Sugianto. (2020). Experimental study on 3D vortex gravitational turbine runner. *AIP Conference Proceedings*, *2296*(1), 020025.
[36] Dakheel, M. H., Khalil, W. H., and Rashid, R. S. (2025). Numerical and experimental investigation of main parameters affecting the performance of micro gravitational water vortex turbine. *AIP Conference Proceedings*, *3303*(1), 120001.
[37] Vinayakumar, B., Antony, R., Binson, V. A., and Youhan, S. (2024). Experimental and numerical study on gravitational water vortex power plant for small water bodies. *e-Prime: Advances in Electrical Engineering, Electronics and Energy, 7*, 100460.
[38] Anshar, A.N., Maulana, A., Nurazizah, S., Nurjihan, Z., Anggraeni, S., and Nandiyanto, A.B.D. (2021). Electrical analysis of combination of orange peel and tamarind for bio-battery application as an alternative energy. *Indonesian Journal of Multidiciplinary Research*, *1*(1), 125-128.
[39] Fauziah, N.R., Maoludin, S.A., Ramadhan, W.S., Wafi, W., Khoerunnisa, F., and Winarno, N. (2021). Geothermal: from education to a new solution for renewable energy. *Indonesian Journal of Multidiciplinary Research*, *1*(1), 85-88.
[40] Hidayah, F., Muslihah, F., Nuraida, I., Winda, R., Vania, V., Rusdiana, D., and Suwandi, T. (2021). Steam power plant powered by wood sawdust waste: A prototype of energy crisis solution. *Indonesian Journal of Teaching in Science*, *1*(1), 39-46.
[41] Irawan, A.K., Rusdiana, D., Setiawan, W., Purnama, W., Fauzi, R.M., Fauzi, S.A., Alfani, A.H.F., and Arfiyogo, M.R. (2021). Design-construction of a solar cell energy water pump as a clean water source for people in Sirnajaya village, Gununghalu district. *ASEAN Journal of Science and Engineering Education*, *1*(1), 15-20.
[42] Jakhongir, S., Kurbonov, K., Muhabbat, H., Salim, K., Shavkat, M., Khulkar, K., and Doniyor, K. (2023). Analyzing climate policy utilizing financial and energy industry models. *ASEAN Journal of Economic and Economic Education*, *2*(2), 125-138.
[43] Juhanaini, J., Sholihat, L.F., Maryanti, R., Budiman, R.A., and Armindony, F.F. (2022). Media learning patch board in science learning energy change materials for children with intellectual disabilities. *Indonesian Journal of Teaching in Science*, *2*(2), 139-146.
[44] Jweri, A.R.K., Ogaili, A.A.F., Amin, S.A., Khalaf, M.I., Al-Haddad, L.A., Jaber, A.A., and Karkhi, M.I. (2025). Enhancing predictive maintenance in energy systems using a hybrid Kolmogorov-Arnold network (KAN) with short-time Fourier transform (STFT) framework for rotating machinery. *ASEAN Journal of Science and Engineering*, *5*(2), 465-494.
[45] Kareem, K., Rasheed, M., Liaquat, A., Hassan, A.M.M., Javed, M.I., and Asif, M. (2022). Clean energy production from jatropha plant as renewable energy source of biodiesel. *ASEAN Journal of Science and Engineering*, *2*(2), 193-198.
[46] Khan, M.A., Hakeem, L., Ali, M.J., and Hussain, M.S. (2025). Uncovering the full potential utilization of petroleum reserves residue for sustainable energy supply. *ASEAN Journal for Science and Engineering in Materials*, *4*(1), 13-22.

DOI: https://doi.org/10.17509/ijost.v11i3.90012
p- ISSN 2528-1410 e- ISSN 2527-8045

[47] Octaviani, H., Sakti, A.W., and Bilad, M.R. (2022). Improving activities and learning outcomes of elementary school students through experimental methods using lime as an alternative electrical energy source during the covid-19 pandemic. *ASEAN Journal for Science Education*, *1*(2), 63-74,

[48] Pechsiri, T., and Puengsungwan, S. (2023). Energy harvesting based on living plants for smart farming. *ASEAN Journal of Science and Engineering*, *3*(1), 47-56.

[49] Putri, B.M., Ningrum, L., and Maulida, N.M. (2021). Simple micro-hydro uses water as a renewable energy source. *Indonesian Journal of Multidiciplinary Research, 1*(1), 23-28.

[50] Sani, S., Siraj, I.T., Kurawa, M.A., and Koki, I.B. (2023). Energy-efficient synthetic method, X-ray diffraction analysis and thermal decomposition of cobalt (II) and nickel (II) schiff base complexes derived from 2-aminobenzothiazole. *ASEAN Journal of Science and Engineering*, *3*(2), 185-198.

[51] Sihombing, D.A., Yulianti, L., and Prima E.C. (2021). Aloe vera as an alternative energy source. *Indonesian Journal of Multidiciplinary Research, 1*(1), 29-34.

[52] Strömberg, L.J. (2023). Electro-magnetism in battery pot plants with heating chambers for heat energy transduction. *ASEAN Journal of Science and Engineering*, *3*(1), 63-68.

[53] Susilowati, N.I., Liliawati, W., and Rusdiana, D. (2023). Science process skills test instruments in the new indonesian curriculum (merdeka): Physics subject in renewable energy topic. *Indonesian Journal of Teaching in Science*, *3*(2), 121-132.

[54] Umar, A., Gbenga, A.A., Yusuf, M.-N. O., Faridah, A., Emmanuel, A.T., and Adekitan, A.F. (2025). Production and characterization of briquettes from agricultural wastes for sustainable energy solutions. *ASEAN Journal for Science and Engineering in Materials*, *4*(2), 121-136.

[55] Waheed, A., Habibullah, H., Irfan, M., Hassan, A., Habib, B., Abbas, S., and Shafique, M.Z. (2024). Exploring diverse substrates for enhanced water splitting: tailoring energy conversion and storage through specific qualities with its limitations. *ASEAN Journal for Science and Engineering in Materials*, *3*(2), 141-176.

DOI: https://doi.org/10.17509/ijost.v11i3.90012
p- ISSN 2528-1410 e- ISSN 2527-8045